

New insight into photoacoustic conversion efficiency by plasmon-mediated nanocavitation: Implications for precision theranostics

Yujiao Shi, Sihua Yang (✉), and Da Xing (✉)

Ministry of Education Key Laboratory of Laser Life Science and Institute of Laser Life Science, College of Biophotonics, South China Normal University, Guangzhou 510631, China

Received: 15 November 2016

Revised: 10 January 2017

Accepted: 14 January 2017

© Tsinghua University Press and Springer-Verlag Berlin Heidelberg 2017

KEYWORDS

photoacoustic imaging, conversion efficiency, nanocavitation, theranostics

ABSTRACT

The probe-assisted integration of imaging and therapy into a single modality offers significant advantages in bio-applications. As a newly developed photoacoustic (PA) mechanism, plasmon-mediated nanocavitation, whereby photons are effectively converted into PA shockwaves, has excellent advantages for image-guided therapy. In this study, by simulating the laser absorption, temperature field, and nanobubble dynamics using both finite-element analysis and computational fluid dynamics, we quantified the cavitation-induced PA conversion efficiency of a water-immersed gold nanosphere, revealing new insights. Interestingly, sequential multi-bubble emission accompanied by high PA signal production occur under a single high-dose pulse of laser irradiation, enabling a cavitation-induced PA conversion efficiency up to 2%, which is ~50 times higher than that due to thermal expansion. The cavitation-induced PA signal has unique frequency characteristics, which may be useful for a new approach for *in vivo* nanoparticle tracking. Our work offers theoretical guidance for accurate diagnosis and controllable therapy based on plasmon-mediated nanocavitation.

Since it was discovered by Bell in 1880 [1], the photoacoustic (PA) effect has been applied in biomedical imaging field as an emerging technology. Benefiting from its capacity for high-resolution sensing of the optical contrast at depths beyond the photon-transport mean free paths, PA imaging provides outstanding opportunities for noninvasively monitoring disease

pathophysiology *in vivo* [2–10]. The PA technique has been employed for various bio-applications, such as visualizing blood-vessel structures and melanoma where intrinsic contrast is available [11–13]. Because many diseases lack PA contrast, the use of exogenous contrast agents that selectively target the region of pathological change allows the PA technique to be

Address correspondence to Sihua Yang, yangsh@sclu.edu.cn; Da Xing, xingda@sclu.edu.cn

extended to functional and molecular imaging [14–22]. Among the contrast agents, plasmonic nanoparticles (PNPs) have attracted intensive research interest because they have strong optical absorption and their peak absorption wavelengths can be finely tuned by inducing localized surface plasmon resonance (LSPR). The conventional mechanism for PNP-mediated PA imaging is thermal expansion, where the nanoparticles absorb laser energy, causing localized volume heating and PA wave emission. However, owing to its low conversion efficiency, the biomedical applications of thermal expansion, especially deep-seated tissue imaging, are severely restricted. As a novel alternative PA conversion mechanism [23, 24], plasmon-mediated nanocavitation provides a substantially higher PA conversion efficiency than thermal expansion. When the PNPs are irradiated by a high-dose laser, their sharp temperature increase may exceed the supercritical temperature of the liquid in the vicinity of the PNPs. Thus, a rapid phase transition occurs in the surrounding liquid, and a nanobubble emerges around the PNPs. The quick expansion and collapse of this bubble lead to large PA wave emission. This efficient transduction from photons to acoustic waves enables highly sensitive PA imaging by providing a bright contrast, meanwhile offering a promising therapeutic strategy through shockwave-induced mechanical damage to targeted cells and/or bubble explosion-induced drug release [25, 26]. Recent reports show that image-guided PA therapy can be achieved by utilizing triggerable PNP-loaded perfluorocarbon droplets, via a combined approach involving imaging and therapy functionalities [27]. However, the lack of quantitative analysis of the cavitation-mediated PA effect hinders its application in accurate disease detection and controllable therapy, and vital issues such as the process, the quantified efficiency of the PA conversion, and the *in situ* PA pressure intensity remain unclear.

In this study, we aimed to advance our basic understanding of the nanocavitation mechanism by performing quantitative simulations of the PA conversion process for a water-immersed gold nanosphere under nanosecond laser irradiation. Analytical and computational methods, including finite element analysis (FEA) and computational fluid dynamics (CFD), were used in our simulation, and the computational

method provided intuitive details that cannot be obtained by experiments [28, 29]. We found that the phase transition-induced bubble formation may occur under a laser energy lower than the safety threshold and that the PA signal amplitude is several times that due to thermal expansion. Interestingly, a secondary bubble emerges after the collapse of the first bubble, resulting in sequential multi-bubble emission upon irradiation by a single laser pulse. We monitored the temperature field and found that it is caused by the obstruction of the sphere-liquid heat exchange by the bubble; thus, the sphere temperature remains higher than the liquid supercritical point when the liquid returns to the sphere surface after the first bubble collapses. The multi-bubble emission acts as an *in situ* nano-ultrasonic transmitter by launching multiple sequential pulses, similar to ultrasound therapy. The synergy between the unique bubble dynamics and the nanocavitation-induced high PA pressure enables a cavitation-induced PA conversion efficiency ~50 times higher than that due to thermal expansion. Our simulation offers theoretical guidance for accurate diagnosis and therapy using the cavitation-mediated PA technique and provides useful information for bubble-mediated blood–brain barrier disruption or the increased cellular uptake of therapeutic drugs through cell-membrane poration. Additionally, the nanocavitation-induced PA signal has unique frequency characteristics that can be exploited to develop a new approach for *in vivo* nanoparticle tracking. The PNP aggregation-induced LSPR coupling that leads to nanocavitation under low-dose laser irradiation is also discussed.

The plasmon-mediated absorption of the pulsed laser and the resulting thermal response are of particular interest for biological applications [30]. When the PNPs are illuminated by the pulsed laser, owing to the strong LSPR, free electrons are excited to a high energy level within 50 fs through photon–electron interactions [31]. Then, the excited electrons nonradiatively release their kinetic energy to the lattice of PNPs through electron–phonon interactions and cause localized heating. Assuming that the PNPs are irradiated by laser with a time-harmonic electric field E with a frequency of ω , the electric-field distribution can be computed using the Helmholtz equation [32]

$$\nabla \times (\mu_r^{-1} \nabla \times E) - k_0^2 \left(\varepsilon_r - j \frac{\sigma}{\omega \varepsilon_0} \right) E = 0 \quad (1)$$

Where μ_r , ε_r , σ , and k_0 are the relative permeability, permittivity, conductivity, and wavenumber, respectively. We consider a water-immersed gold nanosphere with a radius of 30 nm, which is rational and practical for biological applications. The electric-field amplitude is $E_0 = 2.4 \times 10^6$ V/m, and the corresponding laser irradiance, $I_{\text{in}} = c\varepsilon_0 n_{\text{water}} E_0^2 / 2$, is ~ 10 mW/ μm^2 , where c , ε_0 , and n_{water} are the speed of light, the vacuum permittivity, and the refractive index, respectively. The interaction of the laser with the PNPs induces polarization and dipolar oscillations of the free electrons in the PNPs [33], and an enhanced electric field appears in the small region around the PNPs, as quantitatively modeled in Fig. 1(a). Through electron-phonon interactions, the sphere transforms kinetic energy into heat, which can be quantitatively computed as resistive heating $Q_{\text{abs}} = J \cdot E$ according to the FEA method [34]. J is the current density due to the free-electron oscillation. The absorbed power as a function

of the incident laser wavelength is calculated in Fig. 1(b), where the wavelength with highest absorption is identified as the plasmon resonant wavelength. The laser absorption of the sphere leads to the heating of the sphere and the surrounding water, and once the water temperature exceeds the supercritical temperature, a phase transition-induced bubble forms around the sphere, as illustrated in Fig. 1(c). Subsequently, thermal energy finally diffuses out of the region of interest.

When the sphere is irradiated by a nanosecond pulsed laser, the quick accumulation of laser energy causes the temperature of the sphere to increase sharply. However, because of the small size of the sphere, its thermal confinement time $\tau_{\text{th}} = R^2/\alpha$ is comparable to the laser pulse width, where R and α are the radius of the sphere and the thermal diffusivity of the liquid, respectively [35]. Thus, the diffusion of thermal energy from the sphere to the surrounding liquid, as well as the increase in the temperature of the liquid, cannot be neglected. Because the laser pulse width is substantially larger than the electron-phonon coupling time, the heat-diffusion equation describes the temperature of

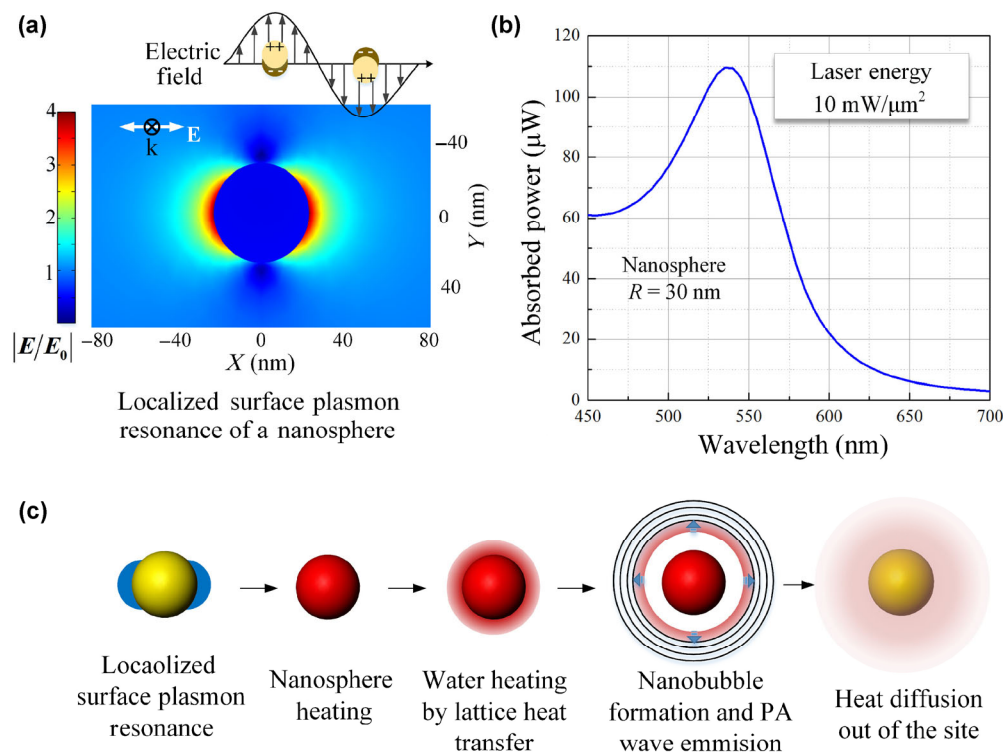


Figure 1 (a) Electric-field enhancement for a 30-nm water-immersed gold nanosphere due to LSPR. The color legend shows the ratio of the enhanced electric field to the incident electric field. (b) Absorbed power as a function of the laser wavelength for the sphere under 10-mW/ μm^2 laser irradiation. (c) Schematic of the PA signal production process based on plasmon-mediated nanocavitation.

the sphere and its surrounding liquid

$$\rho C_p \frac{\partial T}{\partial t} = k \nabla^2 T + Q_{\text{abs}}(t) \quad (2)$$

Where ρ , C_p , k , and T are the density, heat capacity, thermal conductivity, and temperature, respectively. Q_{abs} is the absorbed power. In our simulations, the sphere is irradiated by a laser with a pulse width of 3 ns at the plasmon resonant wavelength, where the liquid (water) is assumed to be optically transparent owing to its relatively low absorption. Figure 2(a) shows the temperature of the sphere with respect to time under laser irradiation of 6 and 20 mW/μm² respectively. For low-dose laser irradiation, the sphere is heated without nanocavitation, and its temperature does not exceed the supercritical temperature of water. The dynamic temperature field is quantitatively simulated, as shown in Fig. 2(b), indicating that the water temperature increases quickly as the laser pulse is applied because of the heat diffusion from the sphere. The length of the heated liquid layer (thermal-diffusion length) is defined as $\chi = \sqrt{\alpha\tau}$ and is ~20.5 nm at the end of the pulsed-laser irradiation. Then, the temperature field is eventually smoothed by heat diffusion. However, for high-dose laser irradiation, the sphere is prone to be overheated, exceeding the supercritical temperature of water (580 K) [32]. Owing to the small size of the sphere, the Laplace pressure [36], $P = 2\sigma/R$, of a 30-nm bubble created by

the liquid surface tension $\sigma = 0.073$ N/m is ~49 atm, resulting in a phase-transition temperature that is substantially higher than the macroscopic boiling temperature of water (373 K). As shown in Figs. 2(a) and 2(c), under the laser irradiation of 20 mW/μm², the sphere and water are gradually heated from 300 K to the supercritical temperature of water within 1.2 ns. Subsequently, a phase transition occurs at the sphere surface: The water first forms a thin vapor layer and then expands into a bubble because the pressure in the vapor is substantially higher than the ambient pressure.

The initial pressure in the newly formed vapor layer can be predicted using the Clausius–Clapeyron equation [37]

$$p_{\text{sat}}(T) = p_0 \exp\left(\frac{H_{\text{vap}}}{R} \left(\frac{1}{T_0} - \frac{1}{T}\right)\right) \quad (3)$$

Here, $p_0 = 101$ kPa and $T_0 = 273.15$ K are the ambient pressure and temperature, respectively, in our simulation, H_{vap} is the latent heat of vaporization, and R is the gas constant. The calculated initial pressure is ~100 atm. The formed vapor layer is in the non-equilibrium state, with a relatively high pressure and temperature. As the expansion continues, the bubble dissipates energy by performing work on the external water, which is accompanied by PA wave emission. The bubble dynamics are simulated by CFD using the Rayleigh–Plesset equation [38]

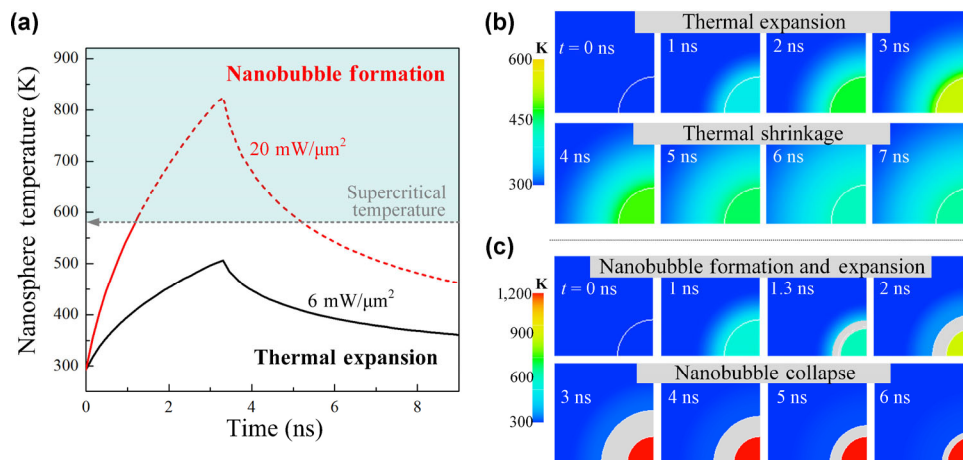


Figure 2 (a) Temperature of the gold nanosphere with respect to time under 3-ns pulsed laser irradiation with different laser energies. (b) Temperature fields for a water-immersed gold nanosphere under 6-mW/μm² laser irradiation. (c) Temperature fields and nanobubble dynamics for a water-immersed gold nanosphere under 20-mW/μm² laser irradiation.

$$\rho \left(R \frac{d^2R}{dt^2} + \frac{3}{2} \left(\frac{dR}{dt} \right)^2 \right) = P_{\text{bubble}} - P_0 - \frac{2\sigma}{R} - \frac{4\mu}{R} \frac{dR}{dt} \quad (4)$$

Here, ρ is the liquid density, R is the bubble radius, μ is the viscosity, and P_{bubble} is the pressure in the bubble. By assuming the bubble to be an ideal gas, the bubble pressure is estimated using the equation of state [32]

$$P_{\text{bubble}} = (\gamma - 1) \rho_{\text{bubble}} C_{\text{bubble,V}} T_{\text{bubble}} \quad (5)$$

Here, $\gamma = C_{\text{bubble,p}}/C_{\text{bubble,V}}$. $C_{\text{bubble,p}}$ and $C_{\text{bubble,V}}$ are the specific heat capacity at a constant pressure and volume, respectively. ρ_{bubble} is dynamically evaluated with respect to the time and temperature in our simulation, and the density, pressure, and temperature are assumed to be homogeneous in the bubble. The expansion of the bubble decreases its internal pressure and temperature, while the pressure of the liquid in the vicinity of the bubble–liquid interface increases because of liquid compression. In our simulation, the liquid pressure is tracked using the volume-of-fluid method according to the Navier–Stokes equation [39]

$$\rho \left(\frac{\partial v}{\partial t} + v \cdot \nabla v \right) = -\nabla P_{\text{liquid}} + \mu \nabla^2 v \quad (6)$$

Here, we assume the liquid (water) to be incompressible and Newtonian. v and P_{liquid} are the velocity and the liquid pressure, respectively. The velocity is assumed

to be continuity in our simulation. After the bubble expands to its maximum radius, it collapses, and the liquid finally returns to the sphere surface (Fig. 2(c)). We assume that during the bubble formation, the power absorbed by the sphere remains constant under the application of the laser pulse. The bubble causes heat insulation between the sphere and the surrounding liquid; thus, a sharp temperature increase is observed from 1.3 to 3 ns. After the application of the laser pulse, no obvious temperature decrease is observed before the bubble collapse.

Through bubble expansion and collapse, the absorbed energy is converted into PA waves, as described by the relationship between the PA pressure and the bubble-induced displacement [40]

$$\nabla P_{\text{PA}} = -\rho \frac{\partial^2 u}{\partial t^2} \quad (7)$$

where P_{PA} and u are the PA wave pressure and the bubble-wall displacement. Equation (7) can be transformed into $P_{\text{PA}} = -\rho c_L \partial u / \partial t$, where c_L is the velocity of sound in the liquid. We quantified the produced PA signal by tracking the bubble-wall displacement, as shown in Fig. 3(a). The bubble expansion corresponds to the compression wave, i.e., the positive part of the PA wave, and the bubble collapse corresponds to the stretch wave, i.e., the negative part of the PA wave. The quick movement of the bubble–liquid interface

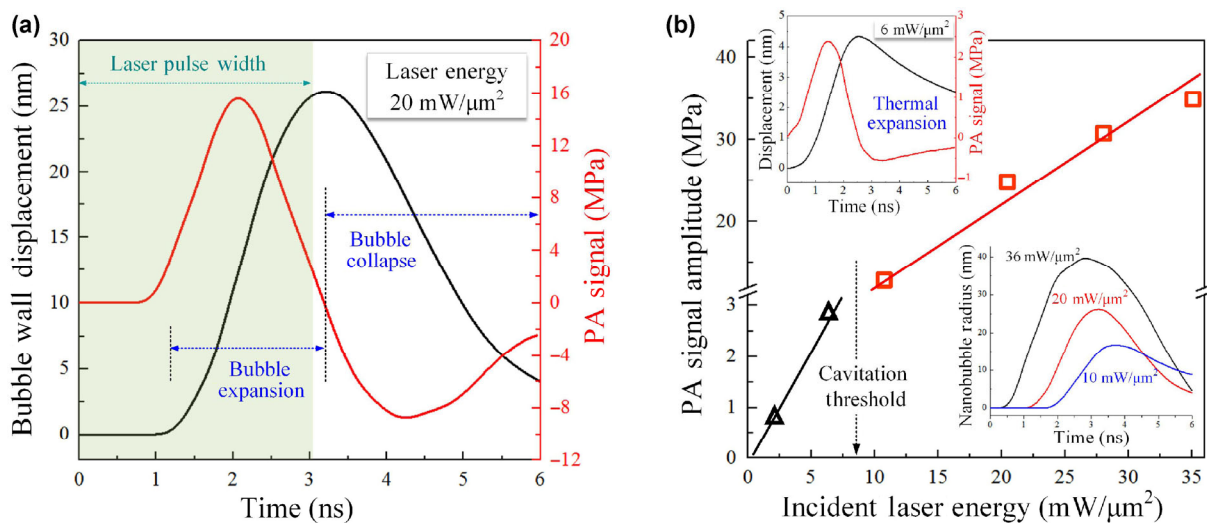


Figure 3 (a) Bubble-wall displacement and PA signal with respect to time. (b) Simulated PA signal amplitudes for a water-immersed gold nanosphere as a function of the incident laser energy.

(~10 m/s) induces the emission of large PA waves with an amplitude of ~25 MPa under 20-mW/μm² irradiation. As the energy of the incident laser increases, the phase transition-induced bubble grows more quickly, and a larger bubble is formed (bottom illustration in Fig. 3(b)), yielding the emission of PA waves with a substantially larger amplitude. In comparison, for a laser energy lower than the cavitation threshold, the PA signal is produced according to the thermal-expansion mechanism. By determining the thermal expansion-induced displacement using FEA method, the produced PA signal can be calculated according to Eq. (7) (top illustration in Fig. 3(b)). This reveals that the nanocavitation produces a substantially higher PA signal amplitude than the thermal expansion. From a microscopic viewpoint, thermal expansion stems from the anharmonicity of the molecular vibration-induced displacement [41], where the molecular spacing in the heated area hardly changes. However, the phase transition due to the bubble formation enlarges the molecular spacing by multiple orders of magnitude, which enables large macroscopic displacement compared with the case of thermal expansion.

Before the bubble collapses, the heat exchange between the sphere and liquid is insulated, and the sphere temperature remains higher than the supercritical temperature. After the bubble collapses and the liquid returns to the sphere surface, the liquid can be heated to the supercritical temperature. Therefore, an interesting phenomenon occurs, where a phase transition and the formation of a secondary bubble follow the collapse of the first bubble, leading to sequential multi-bubble emission upon irradiation by one laser pulse, which lasts until the sphere temperature decreases below the supercritical temperature (Fig. 4(a)). Subsequently, the sphere temperature decreases because of the fast heat diffusion that occurs when the sphere contacts the liquid; here, we hardly observe a temperature gradient in the liquid. Finally, the thermal energy in the sphere is smoothed through the heat diffusion (35.5 ns). The multi-bubble emission causes the multistage oscillation of the PA signal, as shown in Fig. 4(b), leading to wave emission for dozens or even hundreds of nanoseconds under irradiation by a nanosecond pulsed laser (Fig. 4(c)).

We quantify the PA conversion efficiency for both

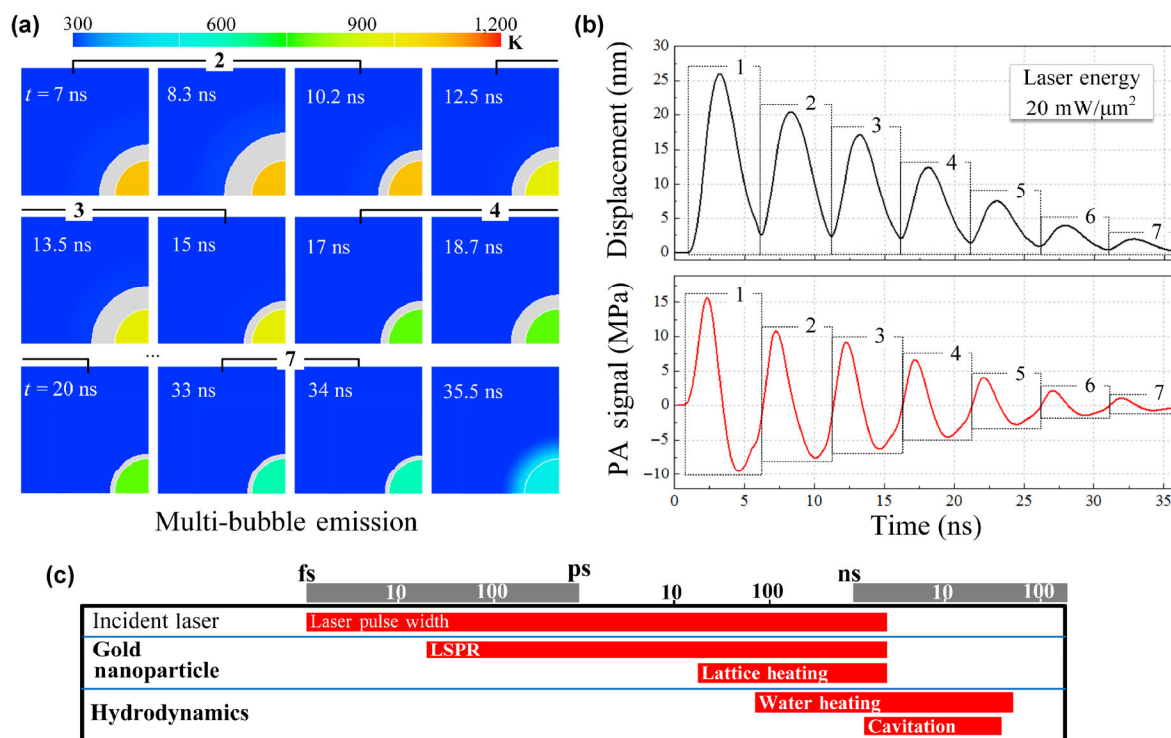


Figure 4 (a) Sequential multi-bubble emission upon irradiation by one laser pulse. (b) Corresponding bubble-wall displacement and PA signal with respect to time. (c) Table showing the time scales of the LSPR, lattice heating, water heating, and cavitation.

thermal expansion [42] and nanocavitation as

$$\eta = W_{\text{bubble}}/W_{\text{laser}} \quad (8)$$

where W_{bubble} is the absorbed laser power, and $W_{\text{laser}} = P_{\text{PA}}^2 S / 8\rho c_L$ is the PA wave power, with S as the wave-emission area.

The multi-bubble emission acts as an *in situ* nano-ultrasonic transmitter by launching multiple sequential pulses. The synergy between the unique bubble dynamics and the nanocavitation-induced high PA pressure leads to an ultrahigh PA conversion efficiency. Figure 5(a) quantitatively compares the PA signal amplitude and the PA conversion efficiency for thermal expansion and nanocavitation under 6 and 20 mW/ μm^2 irradiation, respectively. The cavitation-induced PA conversion efficiency is up to ~2%, which is ~50 times higher than that for thermal expansion. For the PNP-mediated nanocavitation, most of the absorbed energy is finally deposited in the system as thermal energy, and this energy may be useful for photothermal therapy. The plasmon-mediated sequential multi-bubble emission due to irradiation by one laser pulse induces the multistage oscillation of the PA signal, which has unique frequency characteristics. Figure 5(b) shows the frequency spectra for the nanocavitation- and thermal expansion-induced PA signals, which were obtained using the Fourier transform. Compared with the thermal expansion, the nanocavitation shows a narrow frequency band with side peaks. Thus, PNPs that induce nanocavitation can be selectively tracked through frequency analysis of their PA signals. This

method can be developed into a new approach for *in vivo* nanoparticle tracking.

As the PNPs target disease-specific cells, they may suffer target- and endocytosis-induced aggregation [43], which can induce nanocavitation under a relatively low laser energy. Under laser irradiation, the LSPR coupling between the adjacent PNPs leads to a significant electromagnetic-field enhancement compared with the case of single nanoparticles, resulting in a large absorption enhancement [44]. Here, we consider the two-sphere coupling model with a sphere radius of 30 nm and a spacing of 6 nm. As shown in Fig. 6(b), we simulated the absorbed power per sphere, where the absorbed power exhibited an increase by a factor of ~4 compared with that without LSPR coupling. The redshift of the absorption spectrum arises from the LSPR coupling of the two nanospheres. Therefore, nanocavitation occurs even under low-dose laser irradiation (6 mW/ μm^2), as shown in Fig. 6(c). However, the nanospheres are overheated at a temperature higher than their melting temperature (~1,300 K) [45, 46]. Owing to their small size, gold nanoparticles have a lower melting temperature than bulk gold (1,337 K). The melting of the nanomaterials should be avoided to ensure their stability in bio-applications. Our discussion provides a theoretical basis for nanocavitation-induced sensitive PA imaging and therapy under low-energy laser irradiation.

We investigated the PA conversion process caused by plasmon-mediated nanocavitation for a water-immersed gold nanosphere under nanosecond laser

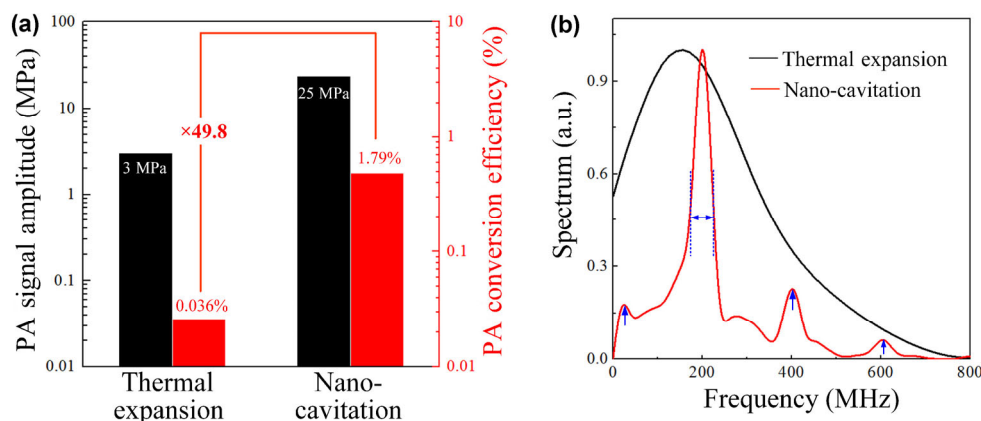


Figure 5 (a) Quantitative comparison of the PA signal amplitude and the PA conversion efficiency for a water-immersed gold nanosphere under the thermal expansion (6 mW/ μm^2) and nanocavitation (20 mW/ μm^2). (b) Normalized frequency spectra of the PA signal produced by the thermal expansion and nanocavitation.

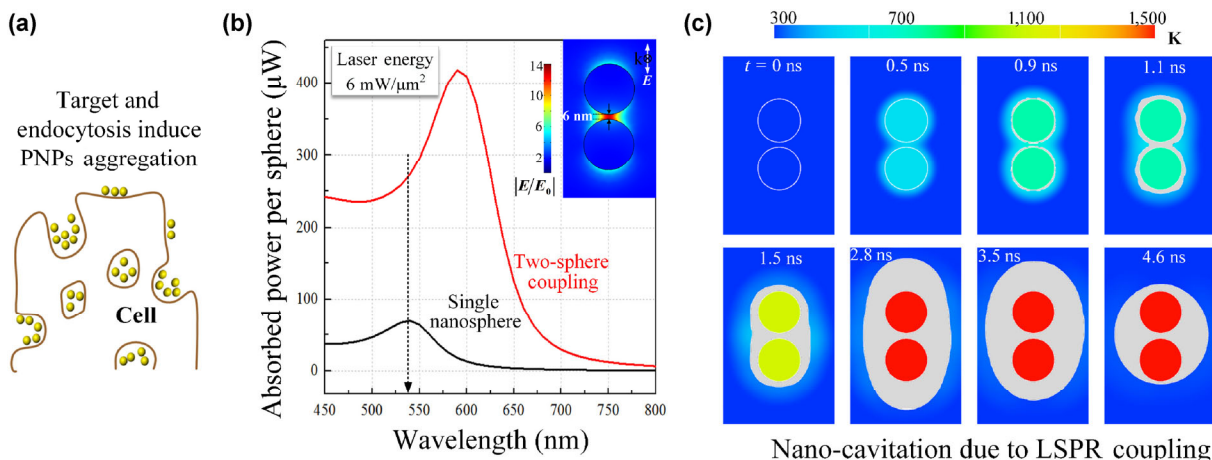


Figure 6 (a) Schematic of target- and endocytosis-induced PNP aggregation. (b) Absorbed power per sphere for two-sphere LSPR coupling. The electric-field enhancement for the two-sphere coupling model with a sphere radius of 30 nm and a spacing of 6 nm is illustrated. (c) Two-sphere coupling-induced nanocavitation under $6\text{-mW}/\mu\text{m}^2$ laser irradiation.

irradiation. In contrast to our mechanism, Meunier et al. [47] reported that plasmon-mediated cavitation can also occur under ultrafast laser irradiation. They used a near-infrared femtosecond laser pulse to induce an enhanced field around the nanoparticles, which directly ionized and heated nanoplasma in the surrounding water, forming a bubble. Because this mechanism strongly depends on the nonlinear energy absorption in water rather than the absorption of the nanoparticles, a substantially higher laser fluence is needed to induce the plasmon-mediated cavitation, which restricts the bio-applications of the method.

The plasmon-mediated nanocavitation is a complicated multiphysics process involving optical-thermal-fluid coupling. Compared with models that simply focus on the spherical bubble dynamics without considering the heat transfer [48], our computational method is more suitable for providing intuitive thermal and bubble-dynamic details, especially for nanoparticles with various shapes.

By simulating the laser absorption, the temperature field, and the nanobubble dynamics using both FEA and CFD, we quantified the cavitation-induced PA conversion efficiency of a water-immersed gold nanosphere and compared it with the thermal expansion-induced PA conversion efficiency. The synergy between the sequential multi-bubble emission under irradiation by a single laser pulse and the large PA signal amplitude yield a PA conversion efficiency

~50 times higher than that for thermal expansion. Additionally, the cavitation-induced PA signal has unique frequency characteristics that can be exploited to develop a new approach for *in vivo* nanoparticle tracking. The PNP aggregation-induced LSPR coupling that leads to nanocavitation under low-dose laser irradiation was also examined. Our simulation offers theoretical guidance for cavitation-mediated accurate diagnosis and therapy using the PA technique.

Acknowledgements

This research is supported by the National Natural Science Foundation of China (Nos. 81630046, 61627827, 61331001, 91539127, and 11604105), the Science and Technology Planning Project of Guangdong Province (Nos. 2015B020233016, 2014B020215003 and 2014A020215031), and the Distinguished Young Teacher Project in Higher Education of Guangdong (No. YQ2015049).

References

- [1] Bell, A. G. On the production and reproduction of sound by light. *Am. J. Sci.* **1880**, *20*, 305–324.
- [2] Zhang, H. F.; Maslov, K.; Stoica, G.; Wang, L. V. Functional photoacoustic microscopy for high-resolution and noninvasive *in vivo* imaging. *Nat. Biotechnol.* **2006**, *24*, 848–851.

- [3] Wang, L. V.; Hu, S. Photoacoustic tomography: *In vivo* imaging from organelles to organs. *Science* **2012**, *335*, 1458–1462.
- [4] Xiang, L. Z.; Wang, B.; Ji, L. J.; Jiang, H. B. 4-D photoacoustic tomography. *Sci. Rep.* **2013**, *3*, 1113.
- [5] Kruger, R. A.; Lam, R. B.; Reinecke, D. R.; Del Rio, S. P.; Doyle, R. P. Photoacoustic angiography of the breast. *Med. Phys.* **2010**, *37*, 6096–6100.
- [6] Fang, H.; Maslov, K.; Wang, L. V. Photoacoustic Doppler effect from flowing small light-absorbing particles. *Phys. Rev. Lett.* **2007**, *99*, 184501.
- [7] Liu, Y. Y.; Yang, X. Q.; Zhu, D.; Shi, R.; Luo, Q. M. Optical clearing agents improve photoacoustic imaging in the optical diffusive regime. *Opt. Lett.* **2013**, *38*, 4236–4239.
- [8] Oraevsky, A. A.; Jacques, S. L.; Tittel, F. K. Measurement of tissue optical properties by time-resolved detection of laser-induced transient stress. *Appl. Opt.* **1997**, *36*, 402–415.
- [9] Zhang, E. Z.; Laufer, J. G.; Pedley, R. B.; Beard, P. C. *In vivo* high-resolution 3D photoacoustic imaging of superficial vascular anatomy. *Phys. Med. Biol.* **2009**, *54*, 1035–1046.
- [10] Zhang, J.; Yang, S. H.; Ji, X. R.; Zhou, Q.; Xing, D. Characterization of lipid-rich aortic plaques by intravascular photoacoustic tomography: *Ex vivo* and *in vivo* validation in a rabbit atherosclerosis model with histologic correlation. *J. Am. Coll. Cardiol.* **2014**, *64*, 385–390.
- [11] Wang, X. D.; Pang, Y. J.; Ku, G.; Xie, X. Y.; Stoica, G.; Wang, L. V. Noninvasive laser-induced photoacoustic tomography for structural and functional *in vivo* imaging of the brain. *Nat. Biotechnol.* **2003**, *21*, 803–806.
- [12] Yang, S. H.; Xing, D.; Zhou, Q.; Xiang, L. Z.; Lao, Y. Q. Functional imaging of cerebrovascular activities in small animals using high-resolution photoacoustic tomography. *Med. Phys.* **2007**, *34*, 3294–3301.
- [13] Galanzha, E. I.; Shashkov, E. V.; Spring, P. M.; Suen, J. Y.; Zharov, V. P. *In vivo*, noninvasive, label-free detection and eradication of circulating metastatic melanoma cells using two-color photoacoustic flow cytometry with a diode laser. *Cancer Res.* **2009**, *69*, 7926–7934.
- [14] Jiang, Y. Y.; Deng, Z. J.; Yang, D.; Deng, X.; Li, Q.; Sha, Y. L.; Li, C. H.; Xu, D. S. Gold nanoflowers for 3D volumetric molecular imaging of tumors by photoacoustic tomography. *Nano Res.* **2015**, *8*, 2152–2161.
- [15] De La Zerda, A.; Zavaleta, C.; Keren, S.; Vaithilingam, S.; Bodapati, S.; Liu, Z.; Levi, J.; Smith, B. R.; Ma, T. J.; Oralkan, O. et al. Carbon nanotubes as photoacoustic molecular imaging agents in living mice. *Nat. Nanotechnol.* **2008**, *3*, 557–562.
- [16] Chen, Y. S.; Frey, W.; Aglyamov, S.; Emelianov, S. Environment-dependent generation of photoacoustic waves from plasmonic nanoparticles. *Small* **2012**, *8*, 47–52.
- [17] Kim, C.; Favazza, C.; Wang, L. V. *In vivo* photoacoustic tomography of chemicals: High-resolution functional and molecular optical imaging at new depths. *Chem. Rev.* **2010**, *110*, 2756–2782.
- [18] Wang, L.; Yang, P. P.; Zhao, X. X.; Wang, H.; Self-assembled nanomaterials for photoacoustic imaging. *Nanoscale* **2016**, *8*, 2488–2509.
- [19] Ray, A.; Wang, X. D.; Lee, Y. E. K.; Hah, H. J.; Kim, G.; Chen, T.; Orringer, D. A.; Sagher, O.; Liu, X. J.; Kopelman, R. Targeted blue nanoparticles as photoacoustic contrast agent for brain tumor delineation. *Nano Res.* **2011**, *4*, 1163–1173.
- [20] Wang, Y. H.; Liao, A. H.; Chen, J. H.; Wang, C. R. C.; Li, P. C. Photoacoustic/ultrasound dual-modality contrast agent and its application to thermotherapy. *J. Biomed. Opt.* **2012**, *17*, 045001.
- [21] Wei, W.; Li, X.; Zhou, Q. F.; Shung, K. K.; Chen, Z. P. Integrated ultrasound and photoacoustic probe for co-registered intravascular imaging. *J. Biomed. Opt.* **2011**, *16*, 106001.
- [22] Liu, Y.; Yin, J. J.; Nie, Z. H. Harnessing the collective properties of nanoparticle ensembles for cancer theranostics. *Nano Res.* **2014**, *7*, 1719–1730.
- [23] Wilson, K.; Homan, K.; Emelianov, S. Biomedical photoacoustics beyond thermal expansion using triggered nanodroplet vaporization for contrast-enhanced imaging. *Nat. Commun.* **2012**, *3*, 618.
- [24] Dixon, A. J.; Hu, S.; Klibanov, A. L.; Hossack, J. A. Oscillatory dynamics and *in vivo* photoacoustic imaging performance of plasmonic nanoparticle-coated microbubbles. *Small* **2015**, *11*, 3066–3077.
- [25] Kang, B.; Yu, D. C.; Dai, Y. D.; Chang, S. Q.; Chen, D.; Ding, Y. T. Cancer-cell targeting and photoacoustic therapy using carbon nanotubes as “Bomb” agents. *Small* **2009**, *5*, 1292–1301.
- [26] Zhou, F. F.; Wu, S. N.; Yuan, Y.; Chen, W. R.; Xing, D. Mitochondria-targeting photoacoustic therapy using single-walled carbon nanotubes. *Small* **2012**, *8*, 1543–1550.
- [27] Zhong, J. P.; Yang, S. H.; Wen, L. W.; Xing, D. Imaging-guided photoacoustic drug release and synergistic chemo-photoacoustic therapy with paclitaxel-containing nanoparticles. *J. Control. Release* **2016**, *226*, 77–87.
- [28] von Maltzahn, G.; Park, J. H.; Agrawal, A.; Bandaru, N. K.; Das, S. K.; Sailor, M. J.; Bhatia, S. N. Computationally guided photothermal tumor therapy using long-circulating gold nanorod antennas. *Cancer Res.* **2009**, *69*, 3892–3900.
- [29] Rothstein, J. P. Slip on superhydrophobic surfaces. *Annu. Rev. Fluid Mech.* **2010**, *42*, 89–109.

- [30] O'Neal, D. P.; Hirsch, L. R.; Halas, N. J.; Payne, J. D.; West, J. L. Photo-thermal tumor ablation in mice using near infrared-absorbing nanoparticles. *Cancer Lett.* **2004**, *209*, 171–176.
- [31] Groeneveld, R. H.; Sprik, R.; Lagendijk, A. Femtosecond spectroscopy of electron–electron and electron–phonon energy relaxation in Ag and Au. *Phys. Rev. B* **1995**, *51*, 11433.
- [32] Furlani, E. P.; Karampelas, I. H.; Xie, Q. Analysis of pulsed laser plasmon-assisted photothermal heating and bubble generation at the nanoscale. *Lab Chip* **2012**, *12*, 3707–3719.
- [33] Ghosh, S. K.; Pal, T. Interparticle coupling effect on the surface plasmon resonance of gold nanoparticles: From theory to applications. *Chem. Rev.* **2007**, *107*, 4797–4862.
- [34] Hatef, A.; Darvish, B.; Dagallier, A.; Davletshin, Y. R.; Johnston, W.; Kumaradas, J. C.; Rioux, D.; Meunier, M. Analysis of photoacoustic response from gold–silver alloy nanoparticles irradiated by short pulsed laser in water. *J. Phys. Chem. C* **2015**, *119*, 24075–24080.
- [35] Calasso, I. G.; Craig, W.; Diebold, G. J. Photoacoustic point source. *Phys. Rev. Lett.* **2001**, *86*, 3550–3553.
- [36] Menger, F. M. Laplace pressure inside micelles. *J. Phys. Chem.* **1979**, *83*, 893.
- [37] Pan, H. H.; Ritter, J. A.; Balbuena, P. B. Examination of the approximations used in determining the isosteric heat of adsorption from the Clausius–Clapeyron equation. *Langmuir* **1998**, *14*, 6323–6327.
- [38] Prosperetti, A. A generalization of the Rayleigh–Plesset equation of bubble dynamics. *Phys. Fluids* **1982**, *25*, 409–410.
- [39] Chorin, A. J. Numerical solution of the Navier–Stokes equations. *Math. Comput.* **1968**, *22*, 745–762.
- [40] Pelivanov, I. M.; Kopylova, D. S.; Podymova, N. B.; Karabutov, A. A. Optoacoustic method for determination of submicron metal coating properties: Theoretical consideration. *J. Appl. Phys.* **2009**, *106*, 013507.
- [41] Samara, G. A.; Morosin, B. Anharmonic effects in KTaO_3 : Ferroelectric mode, thermal expansion, and compressibility. *Phys. Rev. B* **1973**, *8*, 1256–1264.
- [42] Shi, Y. J.; Qin, H.; Yang, S. H.; Xing, D. Thermally confined shell coating amplifies the photoacoustic conversion efficiency of nanoprobles. *Nano Res.* **2016**, *9*, 3644–3655.
- [43] Albanese, A.; Chan, W. C. Effect of gold nanoparticle aggregation on cell uptake and toxicity. *ACS Nano* **2011**, *5*, 5478–5489.
- [44] Hatef, A.; Meunier, M. Plasma-mediated photothermal effects in ultrafast laser irradiation of gold nanoparticle dimers in water. *Opt. Express* **2015**, *23*, 1967–1980.
- [45] Buffat, P.; Borel, J. P. Size effect on the melting temperature of gold particles. *Phys. Rev. A* **1976**, *13*, 2287–2298.
- [46] Koga, K.; Ikeshoji, T.; Sugawara, K. I. Size- and temperature-dependent structural transitions in gold nanoparticles. *Phys. Rev. Lett.* **2004**, *92*, 115507.
- [47] Boulais, É.; Lachaine, R.; Meunier, M. Plasma-mediated nanocavitation and photothermal effects in ultrafast laser irradiation of gold nanorods in water. *J. Phys. Chem. C* **2013**, *117*, 9386–9396.
- [48] Brujan, E. A. Stress wave emission from plasmonic nanobubbles. *J. Phys. D: Appl. Phys.* **2016**, *50*, 015304.